INTERNATIONAL EDUCATIONAL APPLIED RESEARCH JOURNAL (IEARJ)
Volume: 02, Issue: 01, Jan 2018
E-ISSN: 2456-6713

CARRIER MOBILITY AND ANOMALOUS PCE HYSTERESIS IN METHYL AMMONIUM LEAD PHOTO CELLS

Cliff Orori Mosiori

Department of Mathematics and Physics, Technical University of Mombasa, P.O. Box 90420-80100, Mombasa, Kenya.

Abstract: *Hybrid perovskite solar cells have been developing at a staggering pace in just a few years with the first perovskite cell reported in 2009 managing about 4% PCE. By 2015, perovskite cells had been certified as having more than 20-percent efficiency. However, a number of questions on methyl ammonium lead trihalide ($CH_3NH_3PbI_3$) absorbers remain unanswered. This includes its varying PCE values obtained through rapid reverse and forward scans that yield anomalous hysterical efficiencies. Already, NREL certified PCE values of $CH_3NH_3PbI_3$ solar cell is classified as "unreliable" and not be justifiable for patenting. Solar efficiency basically relies on the behavior of I-V characteristic curve. Such revelations require consistent experimental investigations to explain how electron or charge mobility traverses through $CH_3NH_3PbI_3$ thin films through consistent reproducible experimental techniques like the solvent-solvent extraction method. Photoluminescence measurements; Atomic Force Microscopy, cross-sectional scanning transmission electron microscopy and Time-of-Flight spectrometry are important paramount investigations that can reveal amazing intrinsic relations to electron mobility and transport mechanisms especially those carried with temperature dependent longitudinal and Hall resistances measurements using the standard four-terminal method.*

Keywords: Photoluminescence; Time-of-Flight spectrometry, perovskite solar cell, PCE efficiencies.

1. INTRODUCTION:

Researchers have come up with a number of new techniques of fabricating perovskite films for solid state applications. Some techniques are well suited for making ultra-thin films that are semi-transparent having a capability of making solar cells of different colors. Perovskites are a class of crystalline materials with excellent light absorption levels and much cheaper to make than the silicon wafers. The crystal structure of $CH_3NH_3PbI_3$ has its CH3NH3+ surrounded by PbI6 octahedra [13] making $CH_3NH_3PbI_3$ to be classified as a perovskite material. Its crystal structure is shown in Figure 1. When such materials are used in solar technology as absorbers, they result into perovskite solar cells and the presence of lead in $CH_3NH_3PbI_3$ makes it a hybrid solar cell. Therefore a perovskite solar cell employs a perovskite structured material as its absorber layer [38]. Thin films of CH3NH3PbI3 have a band gap between 1.5 - 2.3 eV depending on its iodide concentration [14] which is a band gap close to an optimal gap for single-junction cells [47, 41]. They also have very strong photon absorption levels [67, 75] in the visible region.

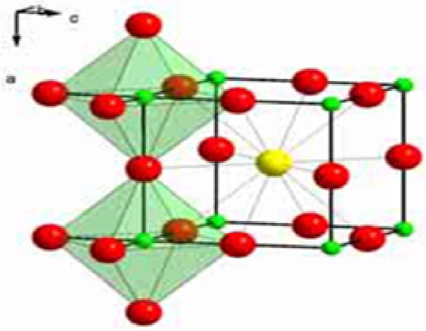

Figure 1: Crystal structure of perosvkite $CH_3NH_3PbI_3$[6]

Already, prototype solar cells have achieved PCE efficiencies ranging from 3.8% [33] in 2009 to 21.0% [9, 58] in 2015. However, by February 2016, the major hurdle that was facing $CH_3NH_3PbI_3$ perovskite solar cell was that their PCE values determined through rapid reverse and forward I-V scans was yielding anomalous hysteric efficiencies. It's generally accepted that the concept behind rapid reverse and forward I-V scans is electron mobility or transfer. Electron transfer is the simplest chemical reaction known in which an electron is transferred from a donor to an acceptor or from a molecular donor state into a particular molecular acceptor state [10] without breaking or creating a chemical bond. It's also generally accepted that the working principles of a solar cell can be explained based on the concept of electron mobility across its junction [22] in which the solar cell's response to electron mobility depends on the density of the electrons or carriers involved, their effective mass [61] and their distribution [35]. However, in $CH_3NH_3PbI_3$ cells, PCE efficiencies are anomalously hysterical and this suggests that the effect of electron mobility on $CH_3NH_3PbI_3$ PCE may be different from the above generally acceptable response in inorganic solar cells.

2. INTRINSIC PARAMETERS IN $CH_3NH_3PBI_3$ SOLAR CELL:

Electron mobility plays an important role on solar cell PCE. The anomalous hysterical efficiencies observed in $CH_3NH_3PbI_3$ solar cells as a result of rapid I-V reverse bias and forward bias scan [5] has become a challenge to NREL in accepting and patenting PCE especially when the scanning parameters exceed the time-scale required for the $CH_3NH_3PbI_3$ layer to attain an electronic steady-state [66, 71]. A number of experimental attempts have been made to normalize these scan I-V curves [47] but they have failed and instead increased the risk of producing inflated PCE values [1]. Some experimental analysis on $CH_3NH_3PbI_3$ solar cells suggest that the likely cause of hysteresis could be due to ion or charge carrier migration or electron mobility [13, 35] without exhaustive describing its effects on hysteresis in PCE of $CH_3NH_3PbI_3$ Perovskite solar cells.

3. $CH_3NH_3PBI_3$ THIN FILM RESEARCH:

In February 2016, NREL revealed that $CH_3NH_3PbI_3$ solar cell based on rapid I-V reverse and forward biased scans were still considered "unreliable" because their PCE efficiencies were anomalously hysterical [20]. This challenge was abided because investigations into the instability of PCE values revealed hysteresis. These investigations proposed that partly, the cause of PCE anomalous hysteresis is due to electron mobility [13, 35] which is a core parameter that determines solar cell efficiency. Questions on how it affects hysteresis started flowing in that required a through investigation for them to be exhaustively understood and explained. Since electron mobility plays a crucial role in solar cell PCE, a thorough investigation to establish the effect of electron mobility on the hysteresis in PCE of $CH_3NH_3PI_3$ perovskite is of essence. A number of parameters need to be reinvestigated. These include: fluorescence measurements to determine $CH_3NH_3PbI_3$ exact concentrations resulting in particular hysterical behavior; optical absorption properties per concentration and growth conditions; Faradic currents through $CH_3NH_3PbI_3$ electrodes using a conventional three-electrode cell to depict electron mobility; electrical and optical transport properties through temperature dependent longitudinal and Hall resistances in a standard four-terminal method. Other proposed investigations include clear and precise elemental compositions measurement using X-ray photoelectron spectroscopy (XPS); determination of apparent free carrier concentration, presence, and location of the confined electrons using Capacitance-Voltage Measurements to unveil scattering centers and photoluminescence measurements at different concentrations, clear valence band structure determinations using ultraviolet photoelectron spectroscopy. Likewise it has been proposed that computation of time of Flight of an electron in relation to threading dislocations in $CH_3NH_3PbI_3$ may reveal striking revelations.

4. REVIEW OF RELATED STUDIES:

A perovskite solar cell functions in a number of different ways depending on the role of its perovskite absorber layer [78] or the nature of its contact electrodes [13]. Perovskite solar cells whose positive charges are extracted by a transparent bottom electrode are classified as either 'sensitized cells' or 'thin-film cells' [10]. In 'sensitized cell' forms, the perovskite layer is believed to function mainly as a light absorber only [40] while charge mobility occurs in other layers [6]. In 'thin-film cell' forms, most of the charge mobility takes place in the bulk perovskite absorber layer itself only [61] and thus, charges are transported through the perovskite layer as light absorption causes charge generation [49]. Perovskite materials were first incorporated into solar cell technology in 2009 [33] using a 'dye sensitized solar cell architecture' achieving 3.8% PCE. In 2011, it achieved 6.5% PCE [28] while a breakthrough was attained in 2012 when a hole transport layer was incorporated [37] resulting into about 10% efficiency. In a 'sensitized cell form' with a TiO_2 architecture [23, 31, 32], the efficiency was above 10%. Further trials [39] only increased open-circuit voltages. In all these literature, the $CH_3NH_3PbI_3$ layer was observed to transport holes [24], electrons [5] and excitons [59, 60]. These observations, convinced solar cell research in perovskite solar cell technology to adopted a thin-film approach in 2013 [6]. The resulting impact was a record efficiency greater than 10% [29] and even exceeding 15% [14, 15] in 2013. Techniques for growing $CH_3NH_3PbI_3$ thin films for solar cells have been evolving. Techniques ranging from thermal evaporation have resulted in solar cells with efficiencies above 15% [11, 25, 39]. More new deposition techniques have been reported in 2014 [8, 17, 18, 21, 34, 50, 51, 54, 57, 63, 68, 74,] corresponding higher PCE. In the mid of 2015 [7, 12, 64, 72] it became apparent that $CH_3NH_3PbI_3$ solar cells function well in a thin-film architecture as proposed by Xiao *et al.* [71] and Noel *et al.*. [47]. In thin-film architecture, it simplified the whole process of determining cell PCE to using rapid reverse and forward biased I-V scans just like in any other inorganic thin film solar cell [27, 55] since normally solar cells PCE is one determined using I-V scans.

Despite all these great achievements, $CH_3NH_3PbI_3$ solar cells have displayed a unique characteristic behavior. Based on their rapid reverse and forward biased scans, a diverse number of ambiguous PCE values have been reported in literature [16, 31, 32, 45, 56]. As an example, Zhou *et al.* [76] reported an efficiency of 19.3% while Snath *et al.* [59, 60] and Unger *et al.* [66] both reported an efficiency of about 21.0% with ambiguous anomalous hysteretic that depended on scanning conditions (scan direction, scan speed, light soaking and biasing). An analysis on these curves by Ahn *et al.* [4] revealed a discrepancy between forward-bias to short-circuit and vice versa that evidently showed hysteresis. A few articles acknowledge hysteretic behavior [1, 17, 18, 31, 32, 46, 47, 49, 59, 60, 57, 73, 75] and fewer agree to slow non-hysteretic I-V curves to little or no hysteresis [71] on extremely slow scans which is believed to allow the system to settle into a steady-state condition [20] to eliminate hysteresis. However, these slow scans fail by yielding lower efficiency values when compared to fast I-V-scans. However, extremely slow voltage-scans which eliminate hysteresis may be holding a key to unfold the anomalous hysteric behaviour. Various propositional explanations have been put forth to be investigated which include but they are not limited to ion movement [13], electric polarization [29, 64], ferroelectric effects [8, 17, 18, 34, 68], large-scale trapping of electrons [24] and filling of trap states [66]. Minemoto, and Murata, [43] investigated the impact of the interface in hole/electron transportation and reported its significance in charge mobility while Lang *et al.* [35] modeled electron transfer using the first principles parameters (e.g. band gap, effective mass etc) and now this work intends to investigate large -scale trapping of electrons and filling of trap states to shade light of electron mobility and transfer mechanisms.

5. MODELING ANALYSIS APPROACHES:

5.1 Redox Reaction Approach:

Already $CH_3NH_3PbX_3$ thin films displays a carrier diffusion length of over one micron [61, 10] enabling its band gap to be tuned by varying its halide concentration [13, 14, 48] in thin film form. However, in its precursor solution, electron behavior can be investigated using its Redox analysis. By applying Nernst Redox reaction equation, its electrochemical potential ($\mu_{e,redox}$) can be taken to be equivalent to its Fermi level ($\mu_{F,redox}$) as:

$$\mu_{F,redox} = \mu_{e,redox} + kT\ln\left(\frac{C_{ox}}{C_{red}}\right) \tag{1}$$

Where C_{ox} and C_{red} = concentration of oxidized and reduced species.

5.2 The Gerischer Model:

As observed in section 3.1 above, already $CH_3NH_3PbX_3$ thin films displays a carrier diffusion length of over one micron which can also be available in its aqueous state. In solution state/solid state interface, when an electron moves from the valence band of a semiconductor to a Redox system [42], the rate of electron mobility is given by;

$$j_v = ek_v^- N_v C_{ox} \tag{2}$$

Were N_v = density of states in the valence band and k_v^- = its rate constant which depends on the density of energy states on both sides of the interface. If N_v is constant, the ratio j_v^- / C_{ox} can be taken as;

$$\mathrm{j}_v^- / C_{ox} = \mathrm{e}\,\mathrm{k}_v^- \mathrm{N}_v \tag{3}$$

Hence, the rate constant, k_v^- in the valence band to be obtained as;

$$k_v^- = \mathrm{k}_0 - \exp\left(\frac{\left(E_v^s + \lambda - E^\circ_{F,redox}\right)^2}{4\lambda\mathrm{kT}}\right) \tag{4}$$

Where k_v^- depends on $E^\circ_{F,redox}$, the edge of the valence band at the semiconductor-electrolyte junction (E_v^s) and energy of the redox (λ). If λ and $E_v^s - E^\circ_{F,redox}$ are known, k_v^- can be calculated. If $E_v^s + \lambda = E^\circ_{F,redox}$ then k_v^- = k_0 and estimates k_v^- = a constant obtained by substituting j_v^- / C_{ox} into Eq. (4) and Eq. (4) using Eq. (5) and Eq. (6) to get;

$$\ln k_v^- = \ln \mathrm{k}_0 - \frac{\left(E_v^s + \lambda - E^\circ_{F,redox}\right)^2}{4\mathrm{kT}\lambda}$$

(5)

$$\ln k_v^- = -\frac{{E^\circ_{F,redox}}^2}{4\mathrm{kT}\lambda} + a$$

(6)

A plot of a curve for $\ln k_v^-$ versus ${E^\circ_{F,redox}}^2$ using Eq. (5) to obtain λ from the slope gives;

$$\ln k_v^- = -\frac{{E^\circ_{F,redox}}^2}{4\mathrm{kT}\lambda} + a = a - \left[\frac{1}{4\lambda\mathrm{kT}}\right]\left(E^\circ_{F,redox}\right)^2 \tag{7}$$

From this curve, the line $\frac{1}{4\lambda\mathrm{kT}}$ can be used to get the value of *a,* as;

$$a = \ln \mathrm{k}_0 - \frac{(E_v^s + \lambda)^2 - 2(E_v^s + \lambda)E^\circ_{F,redox}}{4\lambda\mathrm{kT}}$$

(8)

5.3 The Lindau-Zener Model:

A non-adiabatic electron transfer [52] can be treated by using the Fermi's Golden Rule (FGR) as a two-atom-electron pump expressed as;

$$k_{ET} = \frac{2\pi V^2 FC}{h} \tag{9}$$

where FC = Franck–Condon factor and V is an electronic coupling term depending on electronic wave function overlaps of in the initial and final states. In this case, charge transfer is limited either by the tunneling rates to the electrodes or between the two donors and thus the transition rate, k_{tr} depends on the height of the energetic barrier (activation energy, E_a) such that the frequency of reaching the crossing area gives a transition coefficient (K) expressed as:

$$k_{tr} = KV\exp(-E_a) \qquad (10)$$

Electron pumping through many donors has been reported in large structures [36]. Motivated by metrological applications, modulation period has been found to be comparable to the characteristic time which particles spend in the system. The transition coefficient, K is also related to the probability of transition in the crossing area (P) by the Landau–Zener equation [70] given as;

$$K = \frac{2P}{(1+P)}$$

Where

$$P = 1 - \exp\frac{4\pi^2 V^2}{hv(S_i - S_f)}$$

(11)

Where V = electronic coupling factor, v = velocity of nuclear motion, S_i and S_f = the slopes of the initial and final terms in the region such that for a small exponent, we have;

$$P = \frac{4\pi^2 V^2}{hv(S_i - S_f)}$$

(12)

This process is called non-adiabatic electron transfer. The model predicts the role played by electronic interaction as characterized by the energetic barrier of acceptor and donor interface. Organic and hybrid materials also experience electron pumping and as such Lindau-Zener model can be used to reveal intrinsic pumping mechanisms in $CH_3NH_3PbI_3$ thin films as hybrid electronic pumping semiconductor perosvkite materials.

5.4 The Zusman and Mukamel Model:

This model uses the Zusman equation to study the effect of solvent dynamics on electron transfer reactions. Organic and hybrid materials have a number of weakly bonded molecules and thus $CH_3NH_3PbI_3$ thin films are such hybrid semiconductor perosvkite materials which can be prepared using aqueous precursor solutions at low temperatures. Since the precursor material is a solution, then by this model, the constant electron transfer rate, (k_{ET}) is expressed as a serial combination of the normal non-adiabatic constant electron transfer rate (k_{NA}) and a solvent-controlled constant electron transfer rate, (k_{SC}) as [16];

$$\frac{1}{k_{ET}} = \frac{1}{k_{SC}} + \frac{1}{k_{NA}} \qquad (13)$$

Such that when $k_{SC} >> k_{NA}$ the overall electron transfer rate is expressed as;

$$k_{NA} = \frac{2\pi}{\hbar}|V|^2 \frac{1}{\sqrt{4\lambda_o \pi k_B T}} \sum_{n\to 0}^{\infty} \exp(-S)\left(\frac{S^n}{n!}\right)\exp\left[\frac{(\Delta_r G + \lambda_o + nhv)^2}{4\lambda_o k_B T}\right] \qquad (14)$$

(*Meaning of symbols in the abbreviation section*). If the polarization relaxation of the solvent is taken as the rate limiting step, then $k_{ET} \approx k_{SC}$ when $k_{SC} << k_{NA}$, it means that the contribution of k_{NA} to the overall constant rate is small, making k_{SC} to be expressed as;

$$k_{SC} = \frac{1}{\tau_S}\sqrt{\frac{\lambda_o}{\pi^3 k_B T}}\sin\left[\frac{\Delta G^{\#}}{\lambda_o}\right]\exp(-\frac{\Delta G^{\#}}{k_B T})$$

(15)

Where $\Delta G^{\#} = \frac{(\Delta_r G + \lambda_o)^2}{4\lambda}$ predicts that the electron's constant transfer rate. A reduced electron transfer time ($\tau^*{}_{ET}$) is defined as;

$$\tau^*{}_{ET,Z} = \sqrt{\frac{1}{\lambda_o k_B T}}\exp\frac{(-\Delta G^{\#}/k_B T)}{k_{ET}}$$

(16)

Therefore when substituting Eq.(17) into Eq.(14) and Eq.(16), we find that;

$$\tau^*{}_{ET,Z} = \frac{\sqrt{\pi^3}}{\lambda_o \sin\left(\pi\sqrt{\frac{\Delta G^{\#}}{\lambda_0}}\right)}\tau_S + \sqrt{\frac{1}{\lambda_0 k_B T}}\frac{\exp(-\Delta G^{\#}/k_B T)}{k_{NA}} \qquad (17)$$

As an approximation in Eq. (13), the constant rate expression reduces to the classical expression with an effective electronic coupling given by $\left|V_{eff} = |V|\exp(-\frac{s}{2})\right|$ making Eq. (17) taking the form of;

$$\tau^*{}_{ET,Z} = \frac{\sqrt{\pi^3}}{\lambda_o \sin\left(\pi\sqrt{\frac{\Delta G^{\#}}{\lambda_0}}\right)}\tau_S + \frac{\hbar}{\sqrt{\pi}}\frac{1}{|V_{eff}|^2}$$

(18)

Although λ_o and $\Delta_r G$ are each temperature dependent, τ^*_{ET} is effectively a linear function of τ_S.

5.5 The Drift-Diffusion Model:

The Drift-Diffusion model is a model used to describe electron diffusion in solar cells. Its simplified assumptions are that; all dopants are ionized (shallow dopants); the Fermi energy is at least 3 *kT* below/above the conduction/valence band edge; all variables are independent of time; and temperature is constant throughout the solar cell as device. Its ten model variables are: ***r***, the charge density; *n*, the electron density; *p*, the hole density; ε, the electric field; *f*, the potential; *E*i, the intrinsic energy; *F*n, the electron quasi-Fermi energy; *F*p, the hole quasi-Fermi energy; *J*n, the electron current density and *J*p, the hole current density. This gives drift and diffusion current equations as [2, 3];

$$J_n = qn\mu_n\varepsilon + qD_n\frac{dn}{dx} \tag{19}$$

$$J_p = qn\mu_p\varepsilon - qD_p\frac{dp}{dx} \tag{20}$$

Respectively where D = diffusion coefficient, η = mobility, and *q* indicate the absolute value of the electronic charge in x direction. Organic and hybrid materials have a number of weakly bonded molecules that allow such diffusion and electron transfer and thus $CH_3NH_3PbI_3$ thin films form good hybrid semiconductor perosvkite material for solar cells.

5.6 Molecular Model of Electron Transfer:

This model is based on the resonance interaction between excited states of a weakly coupled aggregate system. Organic and hybrid materials have a number of weakly bonded molecules. Since $CH_3NH_3PbI_3$ thin films are such hybrid semiconductor perosvkite materials, such weakly coupled systems may exist in hybrid thin films since some of them conduct using excitons. Electron mobility depends on whether the system consists of atomic ions or molecular units, nature of external disturbance, nature of external interaction, strength of intermolecular interaction, structure of the aggregate and on the nature of interacting excited states [30]. The rate of transfer for strong coupling exciton is expressed as in Eq. (21) that of weak- coupling as Eq. (25) and for Continuum interaction as Eq. (23)

$$n \sim \left(\frac{f}{r^3}\Theta(\theta)\right) \tag{21}$$

$$n \sim \left(\frac{f}{r^3}\Theta(\theta)\right)\underline{\sum\nolimits_{v,v'} g^*_v g_v S^2_{v,v'}} \tag{22}$$

$$n \sim \left(\frac{f}{r^3}\Theta(\theta)\right)\frac{\sum\nolimits_{v,v'} g_v * g_v S^2_{v,v'}}{\Delta\varepsilon'} \tag{23}$$

Where, f = oscillator strength, Θ(*θ*) = angular dependence of the dipole-dipole interaction, r = distance between interacting centres, n = transfer rate, v'= vibrational level of non-excited molecule; v = vibrational level of excited molecule, g_v'= population level of excited molecule; g_v = population level of non-excited molecules; Δε = rate of individual vibronic band width and S= lowest binding energy.

6. GROWTH PROCEDURES:

A number of techniques have been utilized to grow $CH_3NH_3PbI_3$ thin films. In general, most of these techniques do not replicate. However, those grown as proposed by Zhou *et al.* [77, 78] have in most cases reproduced it intrinsic characteristics. This method is now referred to as the *Solvent-Solvent Extraction Method*. In his method, perovskite precursors are dissolved in a solvent called NMP and coated onto a substrate and then the substrate is bathed in diethyl ether (DEE), which is a second solvent that selectively grabs the NMP solvent and whisks it away leaving an ultra-smooth film of perovskite crystals.

7. CHARACTERIZATION TECHNIQUES:

7.1 Faradic current conductivity measurements:

One technique that is rare utilized in analyzing $CH_3NH_3PbI_3$ is the AC impedance analysis. This method employs the Gamry Interface electrochemical instrument especially the four point probe using in-line four-point probe configuration. It is a technique that applies the Gerischer Model of electron transfer to relate and explain electron transfer in many Redox systems especially those created at the interface between thin film and an electrolyte. Acidic proton exchange membranes (PEM) have been used in fuel cells because of their high proton conductivity and mechanical stability. Furthermore, these membrane materials are rather easily available as they are widely used in chlor-alkali electrolysis, which also helped their adoption into fuel cells. By adding the ionomer in the catalyst layer [36], which provided the necessary proton conductivity, the reaction interface is extended from the catalyst-membrane interface into the catalyst layer. This made the membrane electrode assembly more efficient with respect to current and power density [46]. The completely solid phase membrane electrode assembly, without the need of any liquid electrolyte, is highly desirable as it avoids heavy corrosion problems within the whole fuel cell system. Several groups have carried out tests on these solid polymeric anion exchange membrane fuel cells [1, 6, 23, 28, 70] Solid alkaline fuel cells are also attractive as they can give reasonable power output with non-noble metal catalysts because of the improved kinetics in alkaline medium and the increased stability of the non-noble metals at higher pH values.

7.2 Film Thickness Measurements:

The geometrical thickness of thin films is simply determined at the edge of a thin film edge by a Stylus Method-Profilometer. Such profilometers are computerized for easy retrieval of data and therefore they are highly sensitive surface profilers that are capable of measuring roughness, step height, and other surface characteristics. The best technique for a specific application' or process, depends upon the film type, the thickness of the film, the accuracy desired, and the use of the film. These criteria include such properties as film thickness, film transparency, film hardness, thickness uniformity, substrate smoothness, substrate optical properties, and substrate size. In many cases there is no single best technique, and the particular one chosen will be determined by the personal preferences of the investigator. One of the most recommended methods for hybrid perosvkite thin films is the Multiple-beam Interferometry. In the case of multiple beam reflection, only the silver film CDEF need be fairly transparent (low absorptivity), whereas for multiple-beam transmission both silver films must have low absorptivities. Multiple-beam interferometry for the measurement of film thickness can be implemented by the method of Donaldson and Kharnsavi [16]. Some organic films are altered by the heat generated during the evaporation of the reflective metal and should not be measured by this technique. The use of Fizeau fringes for thickness measurements is commonly called the Tolansky technique in recognition of Tolansky's contributions to the field of multiple-beam interferometry. The sample, channel size, wedge angle, etc., are exaggerated for illustrative purposes and not drawn to scale. The film thickness is given by $d = \Delta N \lambda /2$ where ΔN is the number of fringes or fraction thereof traversing the step. In the interferogram shown in Fig. 3, the depth of the channel (the film thickness) is exactly one-half of the separation between fringes ($\Delta N = 0.5$), and therefore the film thickness is $\lambda/4$. If the wavelength were that of the green mercury line, the film thickness would be 1,365 A^0.

It is sometimes preferable to give the order as $N = 2t\nu$, where ν is the reciprocal wavelength or the frequency in wave numbers, as this relation shows N to be linear with wave number. However, this linearity is not found to be exactly true if the phase changes at the two reflecting interfaces vary with wavelength. Hence, there may be a slight dispersion with wavelength, but the effect of phase change on the determined fringes is very small. This has been treated more extensively by Bennett. It is therefore necessary to deduce t as well as N from the wavelengths of the observed fringes. If N_1 is the order of a fringe corresponding to wavelength λ_1, then $N_1 + 1$ is the order of the next fringe with a shorter λ_o on the interferogram. Neglecting the small phase-change dispersion, we solve for N_1 we obtain;

$$N_1\lambda_1 = (N_1 + 1)\lambda_0 = 2t \tag{28}$$

$$N_1 = \frac{\lambda_0}{\lambda_1 - \lambda_0} \tag{29}$$

And can now express t solely in terms of measured wavelengths:

$$t = \frac{N_1\lambda_1}{2} = \frac{\lambda_1\lambda_0}{2(\lambda_1 - \lambda_0)}$$

(30)

To determine the film thickness, consider that a channel of depth d causes the fringe of the order N_1 to be displaced to a new wavelength λ_1 consequently the film thickness d must satisfy the relation;

$$t + d = \frac{N_1\lambda_1^{'}}{2}$$

(31)

Thus, the film thickness d is given by

$$d = \frac{N_1\lambda_1^{'}}{2} - \frac{N_1\lambda_1}{2} = \frac{\lambda_1^{'} - \lambda_1}{2}\frac{\lambda_0}{\lambda_1 - \lambda_0}$$

(32)

In fig. 5 b and d, the fringe displacements due to the channel are clearly related to the order N of the fringes outside the channel . However if the slop were so steep that the order in the channel could not be related ti that outside the channel, the film thickness could still be derived from the equation;

$$d = \frac{1}{2}(N_1^{'}\lambda_1^{'} - N_1\lambda_1)$$

(33)

Whereby the unknown order N_1' must be obtained by observation of a second displaced fringe of order $N_1' + 1$ as in Eq. (28).

7.3 Transmittance and reflectance Measurement:

A spectrophotometer is currently the most popular instrument used to measure transmittance, reflectance and hence determine absorbance of photon. Data from this measurement is usually in the form of transmittance and reflectance. A number of software based on optical models are employed to analyze data. As a way of explain the data, simulated curves are fitted by a computer program running these models and from such curves, optical spectra interpretation, film thickness, free carrier density, band gap, and free carrier mobility are determined. The problem of determining the film thickness and dispersion properties of optical constants is usually solved by analyzing experimental spectra of the reflection and/or transmission for film-on-substrate structures of interest. Results of the analysis depend on a choice of physical model connecting experimentally measured spectra with geometrical and optical parameters of the structure under study. In order to obtain some reliable relations for practical calculations, as applied to processing of the results of measurements, it is necessary to develop a physically correct model of the thin-film structure, allowing interference and absorption in both the film and substrate materials. Various physical approaches and mathematical models describing the optical spectra for thin-film structures can be found in the literature. They usually present identical results in complicated forms difficult for comparison [1, 27]. A wide variety of different formulae available in the literature, which have been also derived by using dissimilar designations, essentially complicate the choice of the application to a given practical problem. The spectral transmittance is obtained by measuring the transmittance of 3 mm-thick glass with film attached to one face. We determined the visible light transmittance, UV transmittance, solar transmittance, solar reflectance, and shading coefficients for four types of film adhered to glass. The measurements can be performed on light incident from the glass surface using a UV-VIS-NIR spectrophotometer with an integrating sphere accessory under the conditions. Data measured by a Fourier transform infrared spectrophotometer can used to calculate the shading coefficients using software. This software supports the calculation of visible light transmittance, UV transmittance, solar transmittance, and solar reflectance for flat glass according to JIS R3106. For these tests, the calculations prescribed in JIS A5759 can be performed in the user-defined mode by entering the weighting coefficients.

7.4 Surface Morphology Measurement:

One of the most contested parameter is the surface physical features of $CH_3NH_3PbI_3$. The surface morphology and roughness is measured by an atomic force microscopy in non-contact atomic force microscopy mode where the tip of the cantilever does not contact the sample surface. In materials science, roughness on a micrometer and nanometer scale plays an important role in contact-related phenomena, such as adhesion. It is also well known that roughness over a wide range of length scales affects the biological response to surfaces, e.g. cell adhesion, morphology, proliferation, and differentiation. The understanding of these cellular behaviors in connection to the surface topography is crucial in the further development of medical implants. Motivated by the demand of substrata to systematically study roughness-related phenomena, methods for the generation of morphological gradients on different roughness scales have been developed at LSST. First a gradient of micrometer roughness-size feature was developed, by slow immersion of a sand-blasted aluminum sheet into a polishing solution. A nanometer roughness feature-size gradient was achieved by immersion of a flat silicon wafer into a silica particle suspension. Both those gradients have been combined to create an orthogonal gradient, in order to study the synergetic effects of both micrometer and nanometer feature-size roughness in any combination. It is possible to observe the surface morphology (quantity of roughness, composition/chemical state/crystalline state) and structure at the necessary scale by appropriately selecting the method of analysis according to the evaluation purpose and desired contents. JFE-TEC also undertakes sample preparation and processing at a low temperature (cryogenic) or in environmental conditions without exposure to the atmosphere as necessary for clear and genuine material section observation. For nano-to-atomic-scale analysis of fine structures such as material sections, we conduct comprehensive evaluations by taking advantage of the appropriate transmission electron microscopy (TEM) and the methods of analysis like the high-angle annular dark field (STEM-HAADF) method, bright field (BF) method, annular bright field (ABF) method and high-resolution transmission electron microscopy (HR-TEM) method, energy-diffused X-ray analysis (EDX), and electron energy loss spectroscopy (EELS). Preparation of samples for observation and focused ion beam (FIB) processing at low temperature (cryo) or under conditions without exposure by FIB and electrolytic polishing are also possible. Observation at low temperature, Lorentz microscopy and 3D tomography are also available. For nano- to atomic-scale analysis of fine structures such as material sections, we conduct comprehensive evaluations by taking advantage of the appropriate transmission electron microscopy (TEM) and the methods of analysis like the high-angle annular dark field (STEM-HAADF) method, bright field (BF) method, annular bright field (ABF) method and high-resolution transmission electron microscopy (HR-TEM) method, energy-diffused X-ray analysis (EDX), and electron energy loss spectroscopy (EELS). Preparation of samples for observation and focused ion beam (FIB) processing at low temperature (cryo) or under conditions without exposure by FIB and electrolytic polishing are also possible. Observation at low temperature, Lorentz microscopy and 3D tomography are also available.

7.5 Photoluminescence (PL) Measurements:

Photoluminescence is light emission from any form of matter after the absorption of photons. Following an excitation, various relaxation processes may occur in which other photons are re-radiated. It is a powerful technique to probe discrete energy levels and to extract valuable information about semiconductor sample composition, quantum well thickness or quantum dot sample monodispersity. An electron that has been excited above the conduction band of a material will eventually fall and recombine to the hole that has been excited below the valance band after losing some energy through releasing a phonon to the lowest available non-radiative energy level. The efficiency of photoluminescence signal is determined by the nature of optical excitation, properties of material. Time periods between absorption and emission may vary ranging from short femto-second-regime for emission involving free-carriers in semiconductors. Observation of PL at a certain energy using a time-resolved fluoresce spectroscopy by A PL microscope can be viewed as indication of its excitation populated excited state as associated with this transition energy. A laser tuned to a wavelength close to the band gap energy of the sample is directed onto the sample. This may be held in a cryostat to facilitate measurements being taken at low temperatures. The sample is oriented such that the reflected laser beam and the PL emission propagate in different directions. The emitted light is directed into a fibre optic cable and then into a spectrometer. A filter may be placed in front of the fibre input to remove any incident laser light. Inside the spectrometer, a diffraction grating diffracts different wavelengths in different directions towards an array of photo-detectors that measure the intensity of each wavelength component. The digital information is interpreted by the computer, which can display a PL spectrum. The spectrum indicates the relative intensities of light of different wavelengths entering the detector.

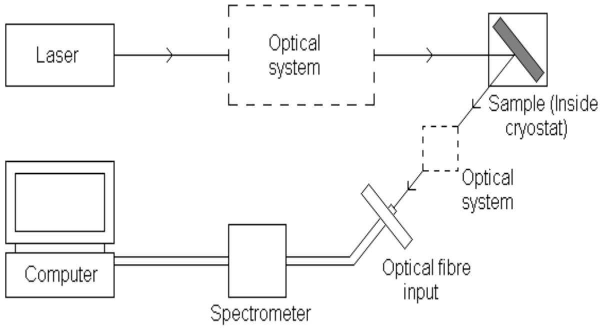

Figure 2: Diagram of PL experiment set-up

Time resolved photoluminescence is a technique that allows the variation in sample PL intensity in response to a laser pulse to be measured over time. The apparatus in figure 2 used is similar to that of standard PL with some differences. The spectrometer is replaced with a monochromator that only selects light of a single wavelength to be directed into a photomultiplier detector capable of single photon counting. The wavelength selected will correspond to that of PL emission from the sample as identified using conventional PL measurements. The CCD input into the computer is also connected to a detector near the output of the laser source, which is used as a trigger for measurement. Laser pulses of ~150fs duration fired at MHz frequency are used in TRPL. On leaving the laser, the pulse acts as a trigger for measurement to begin at the CCD input. Once it is incident on the sample, the pulse will induce PL emission, whose intensity will decay over time before the next pulse hits. The photon count arriving at the detector over short time intervals is recorded, allowing the computer to plot a light intensity decay curve for light of a particular wavelength.

7.6 Fluorescence measurements:

Fluorescence is a member of the ubiquitous luminescence family of processes in which susceptible molecules emit light from electronically excited states created by absorption of light or chemical mechanism. Generation of luminescence through excitation of a molecule by ultraviolet or visible light photons is a phenomenon termed photoluminescence, which is formally divided into two categories, fluorescence, and phosphorescence, depending upon the electronic configuration of the excited state and the emission pathway. Fluorescence is the property of some atoms and molecules to absorb light at a particular wavelength and to subsequently emit light of longer wavelength after a brief interval, termed the fluorescence lifetime. The process of phosphorescence occurs in a manner similar to fluorescence, but with a much longer excited state lifetime. The fluorescence process is governed by three important events, all of which occur on timescales that are separated by several orders of magnitude. Its analysis is best plotted in Joblonski Energy diagrams figure illustrated in 3. Excitation of a susceptible molecule by an incoming photon happens in femtoseconds (10×10^{-15} seconds), while vibrational relaxation of excited state electrons to the lowest energy level is much slower and can be measured in picoseconds (10×10^{-12} seconds). The final process, emission of a longer wavelength photon and return of the molecule to the ground state, occurs in the relatively long time period of nanoseconds (10×10^{-9} seconds). Although the entire molecular fluorescence lifetime, from excitation to emission, is measured in only billionths of a second, the phenomenon is a stunning manifestation of the interaction between light and matter that forms the basis for the expansive fields of steady state and time-resolved fluorescence spectroscopy. Because of the tremendously sensitive emission profiles, spatial resolution, and high specificity of fluorescence investigations, the technique is rapidly becoming an important tool in hybrid perovskite material investigation. In fluorescence, the species is first excited, by absorbing a photon, from its ground electronic state to one of the various vibrational states in the excited electronic state.

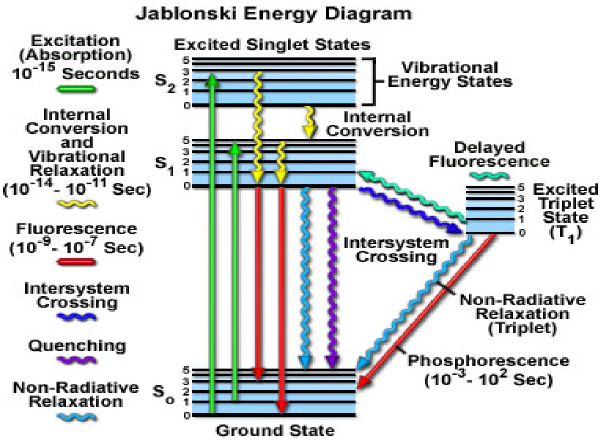

Figure 3: Joblonski Energy diagram

Collisions with other molecules as illustrated in figure 3 cause the excited molecule to lose vibrational energy until it reaches the lowest vibrational state of the excited electronic state. Some of these transitions will have a much higher degree of probability than others, and when combined, will constitute the absorption spectrum of the molecule and may require that you explain them by plotting Franck-.Condon Energy diagrams as illustrated in figure 4.

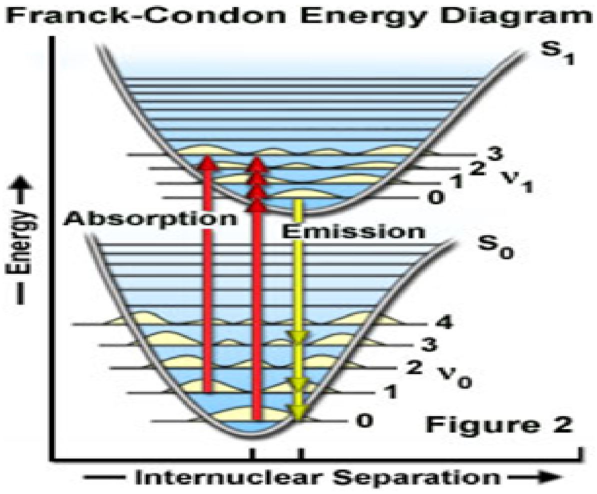

Figure 4: The Franck-.Condon Energy diagram

Note the absorption and excitation spectra are distinct, but often overlap and can sometimes become indistinguishable and as such the absorption and excitation spectra are clearly separated. Immediately following absorption of a photon, several processes will occur with varying probabilities, but the most likely will be relaxation to the lowest vibrational energy level of the first excited state. Such investigations to reveal the behavior of an excited electron in the precursor solution of $CH_3NH_3PbI_3$ and thus represented in the Jablonski diagrams has not been fully investigated. This may unfold the less understood electron transitions in aqueous state and concentrations of $CH_3NH_3PbI_3$p Perosvkite thin films.

7.7 Time-of-flight Measurements:

Time-of-flight mass spectrometry is a method in which an ion's mass-to-charge ratio is determined through a time measurement by accelerating ions using an electric field of known strength. It is carried out using *Time-of-Flight* analyzer. Time-of-flight measurements are often used for measurement of some distance, e.g. with a Laser range finder, used e.g. in an airplane, possibly in the form of a scanning laser radar. Here, an apparatus sends out a short optical pulse and measures the time until a reflected portion of the pulse is monitored. The distance is then calculated using the velocity of light. Due to this high velocity, the temporal accuracy must be rather high – e.g. one nanosecond for a spatial accuracy of 15 cm. The time-of-flight method is typically used for large distances like hundreds of meters or many kilometers. Using advanced techniques it is possible to measure e.g. the distance between earth and the moon with an accuracy of a few centimeters, or to obtain a precise profile of a dam. Typical accuracies of simple devices for short distances are a few millimeters or centimeters. As time-of-flight measurements are preferentially used for large distances, the Beam Quality of the laser Source is crucial. In addition, a telescope can be used to obtain a large Beam Diameter and an accordingly increased Rayleigh length. The target can be equipped with a reflector in order to increase the amount of reflected light. The used pulse duration is usually between 100 ps and a few tens of nanoseconds, as achieved with a Q-switched laser. For large distances, large pulse energies are required. This can raise laser safety issues, particularly if the laser Wavelength is not in the eye-safe region. For nanojoule to microjoule pulse energies, it is possible to use a passively Q-switched microchip Er:Yb:glass laser, which can generate rather short Pulses with pulse energies around 10 µJ in the eye-safe spectral region.

8. CONCLUSION:

A number of parameters that have raised eye blows in the study of $CH_3NH_3PbI_3$ thin films as a potential material for fabricating various optoelectronic devices has been highlighted and therefore need to be reinvestigated. These include fluorescence measurements to determine $CH_3NH_3PbI_3$ exact concentrations resulting in particular hysterical behavior; optical absorption properties per concentration and growth conditions; Faradic currents through $CH_3NH_3PbI_3$ electrodes using a conventional three-electrode cell to depict electron mobility; electrical and optical transport properties through temperature dependent longitudinal and Hall resistances in a standard four-terminal method, elemental compositions measurement using X-ray photoelectron spectroscopy (XPS); and photoluminescence measurements at different concentrations, clear valence band structure determinations using ultraviolet photoelectron spectroscopy and equally computational of time of Flight investigations.

BIBLIOGRAPHY:

The author is a PhD student at Kenyatta University in Hybrid semiconductor materials and doubles up as a lecturer and researcher in Physics of Materials at Technical University of Mombasa.

Acknowledgement:

The author acknowledges the input of his colleagues in the department of Mathematics and Physics of Technical University of Mombasa, Maasai Mara University, Coast Technical Institute and Rift valley Institute of Science and Technology.

REFERENCES:

I. Abate, A.; Saliba, M.; Hollman, J.; Stranks, D.; Wojciechowski, K,; Avolio, R.; Grancini, G.; Petrozza, A.; and Snaith, J. (2014). "Supramolecular Halogen Bond Passivation of Organic–Inorganic Halide Perovskite Solar Cells". Nano Letters 14 (6): 3247–3254.

II. Agarwal, S. and Nair, P. (2014). "Performance optimization for Perovskite based solar cells". Photovoltaic Specialist Conference (PVSC), IEEE 40th: 1515–1518.

III. Agarwal, S. and Pradeep, R. (2015). "Device engineering of perovskite solar cells to achieve near ideal efficiency". Applied Physics Letters 107 (12): 123901.

IV. Ahn, N., Son, D. Y., Jang, I. H., Kang, S. M., Choi, M., & Park, N. G. (2015). Highly reproducible perovskite solar cells with average efficiency of 18.3% and best efficiency of 19.7% fabricated via Lewis base adduct of lead (II) iodide. Journal of the American Chemical Society, 137(27), 8696-8699.

V. Ball, M.; Lee, M.; Hey, A.; and Snaith, J. (2013). "Low-temperature processed meso-superstructured to thin-film perovskite solar cells". Energy & Environmental Science 6 (6): 1739.

VI. Burschka, J.; Pellet, N.; Moon, S.; Humphry-Baker, R.; Gao, P.; Nazeeruddin, K. and Grätzel, M. (2013). "Sequential deposition as a route to high-performance perovskite-sensitized solar cells". Nature 499 (7458): 316–319.

VII. Carlos, F. and Ignacio G. (2008) Revisiting the Effects of the Molecular Structure in the Kinetics of Electron transfer of Quinones: Kinetic Differences in Structural Isomers; J. Mex. Chem. Soc. 52(1), 11-18ISSN 1870-249X

VIII. Chen, H. W., Sakai, N., Ikegami, M., & Miyasaka, T. (2014). Emergence of hysteresis and transient ferroelectric response in organo-lead halide perovskite solar cells. The Journal of Physical Chemistry Letters, 6(1), 164-169.

IX. Collavini, S., Völker, S. and Delgado, L. (2015). "Understanding the Outstanding Power Conversion Efficiency of Perovskite-Based Solar Cells". Angewandte Chemie International 54 (34): 9757–9759.

X. D'Innocenzo, V.; Grancini, G.; Alcocer, J.; Kandada, S.; Stranks, D.; Lee, M.; Lanzani, G. and Snaith, J. (2014). "Excitons versus free charges in organo-lead tri-halide perovskites". Nature Communications 5.

XI. Docampo, Pablo; Ball, James M.; Darwich, Mariam; Eperon, Giles E. and Snaith, J. (2013). "Efficient organometal trihalide perovskite planar-heterojunction solar cells on flexible polymer substrates". Nature Communications 4.

XII. Dualeh, A., Moehl, T., Tétreault, N., Teuscher, J., Gao, P., Nazeeruddin, M. K., & Grätzel, M. (2013). Impedance spectroscopic analysis of lead iodide perovskite-sensitized solid-state solar cells. ACS Nano, 8(1), 362-373.

XIII. Eames, C.; Frost, M.; Barnes, F.; Regan, C.; Walsh, A. and Islam, S. (2015). "Ionic transport in hybrid lead iodide perovskite solar cells". Nature Communications 6: 7497.

XIV. Eperon, E.; Burlakov, M.; Docampo, P.; Goriely, A. and Snaith, J. (2014). "Morphological Control for High Performance, Solution-Processed Planar Hetero-junction Perovskite Solar Cells". Advanced Functional Materials 24 (1): 151–157.

XV. Eperon, E.; Stranks, D.; Menelaou, C.; Johnston, B.; Herz, M. and Snaith, J. (2014). "Formamidinium lead trihalide: a broadly tunable perovskite for efficient planar heterojunction solar cells". Energy & Environmental Science 7 (3): 982.

XVI. Filipič, M.; Löper, P.; Niesen, B.; Wolf, S.; Krč, J.; Ballif, C. and Topič, M. (2015). "CH3NH3PbI3 perovskite/silicon tandem solar cells: characterization based optical simulations". Optics Express 23 (7)

XVII. Frost, J. M., Butler, K. T., & Walsh, A. (2014). Molecular ferroelectric contributions to anomalous hysteresis in hybrid perovskite solar cells. Apl Materials, 2(8), 081506.

XVIII. Frost, J. M., Butler, K. T., Brivio, F., Hendon, C. H., Van Schilfgaarde, M., & Walsh, A. (2014). Atomistic origins of high-performance in hybrid halide perovskite solar cells. Nano letters, 14(5), 2584-2590.

XIX. Heo, J. H., Song, D. H., Han, H. J., Kim, S. Y., Kim, J. H., Kim, D., .. & Im, S. H. (2015). Planar CH3NH3PbI3 perovskite solar cells with constant 17.2% average power conversion efficiency irrespective of the scan rate. Advanced Materials, 27(22), 3424-3430.

XX. Giles, R., Simon E. J., Ralf G. N., Timo A. P., Jamie M. F., Petra J. C. and Alison B. W. (2016) Can slow-moving ions explain hysteresis in the current–voltage curves of perovskite solar cells? Energy Environ. Sci., 9, 1476-1485.

XXI. Gonzalez-Pedro, V.; Juarez-Perez, J.; Arsyad, W.; Barea, M.; Fabregat-Santiago, F.; Mora-Sero, I. and Bisquert, J. (2014). "General Working Principles of CH3NH3PbX3 Perovskite Solar Cells". Nano Letters 14 (2): 888–893.

XXII. Habisreutinger, S. N., Leijtens, T., Eperon, G. E., Stranks, S. D., Nicholas, R. J., & Snaith, H. J. (2014). Carbon nanotube/polymer composites as a highly stable hole collection layer in perovskite solar cells. Nano letters, 14(10), 5561-5568.

XXIII. Hadlington, S. (2012). "Perovskite coat gives hybrid solar cells a boost", RSC Chemistry world.

XXIV. Hao, F., Stoumpos, C. C., Liu, Z., Chang, R. P., & Kanatzidis, M. G. (2014). Controllable Perovskite Crystallization at a Gas–Solid Interface for Hole Conductor-Free Solar Cells with Steady Power Conversion Efficiency over 10%. Journal of the American Chemical Society, 136(46), 16411-16419.

XXV. Haruyama, J., Sodeyama, K., Han, L., & Tateyama, Y. (2014). Termination dependence of tetragonal CH3NH3PbI3 surfaces for perovskite solar cells. The Journal of Physical Chemistry Letters, 5(16), 2903-2909.

XXVI. Jeon, N. J., Lee, H. G., Kim, Y. C., Seo, J., Noh, J. H., Lee, J., & Seok, S. I. (2014). O-Methoxy substituents in spiro-OMeTAD for efficient inorganic–organic hybrid perovskite solar cells. Journal of the American Chemical Society, 136(22), 7837-7840.

XXVII. Jeon, N.; Noh, H.; Kim, C.; Yang, S.; Ryu, S. and Seok, I. (2014). "Solvent engineering for high-performance inorganic–organic hybrid perovskite solar cells". Nature Materials 13 (9): 897–903.

XXVIII. Jeong-Hyeok I.; Lee, C.; Lee, J.; Park, S. and Park, N. (2011). 6.5% efficient perovskite quantum-dot-sensitized solar cell". Nanoscale 3 (10): 4088–93.

XXIX. Juarez-Perez, E. J., Sanchez, R. S., Badia, L., Garcia-Belmonte, G., Kang, Y. S., Mora-Sero, I., & Bisquert, J. (2014). Photoinduced giant dielectric constant in lead halide perovskite solar cells. The Journal of Physical Chemistry Letters, 5(13), 2390-2394.

XXX. Kasha, M. (2012). Energy Transfer Mechanisms and the Molecular Exciton Model for Molecular Aggregates1, 2. Radiation research, 178(2), AV27-AV34.

XXXI. Kim, H. S., & Park, N. G. (2014). Parameters affecting I–V hysteresis of CH3NH3PbI3 perovskite solar cells: effects of perovskite crystal size and mesoporous TiO2 layer. The Journal of Physical Chemistry Letters, 5(17), 2927-2934.

XXXII. Kim, H.; Lee, C.; Im, J.; Lee, K.; Moehl, T.; Marchioro, A.; Moon, S.; Humphry-Baker, R.; Yum, J.; Moser, E.; Grätzel, M. and Park, N. (2012). "Lead Iodide Perovskite Sensitized All-Solid-State Submicron Thin Film Mesoscopic Solar Cell with Efficiency Exceeding 9%". Scientific Reports 2.

XXXIII. Kojima, A.; Teshima, K.; Shirai, Y. and Miyasaka, T, (2009). "Organometal Halide Perovskites as Visible-Light Sensitizers for Photovoltaic Cells". Journal of the American Chemical Society 131 (17): 6050–6051.

XXXIV. Kutes, Y., Ye, L., Zhou, Y., Pang, S., Huey, B. D., & Padture, N. P. (2014). Direct observation of ferroelectric domains in solution-processed CH3NH3PbI3 perovskite thin films. The journal of physical chemistry letters, 5(19), 3335-3339.

XXXV. Lang, L.; Yang, J.; Liu, H.; Xiang, J. and Gong, G. (2014). First-principles study on the electronic and optical properties of cubic ABX3 halide perovskites. Physics Letters A 378 (3): 290–293.

XXXVI. Lansbergen, G. P., Ono, Y., & Fujiwara, A. (2012). Donor-based single electron pumps with tunable donor binding energy. Nano letters, 12(2), 763-768.

XXXVII. Lee, M.; Teuscher, J.; Miyasaka, T.; Murakami, N. and Snaith, J. (2012). "Efficient Hybrid Solar Cells Based on Meso-Superstructured Organometal Halide Perovskites". Science 338 (6107): 643–647.

XXXVIII. Leguy, A. M., Hu, Y., Campoy-Quiles, M., Alonso, M. I., Weber, O. J., Azarhoosh, P., & Docampo, P. (2015). Reversible hydration of CH3NH3PbI3 in films, single crystals, and solar cells. Chemistry of Materials, 27(9), 3397-3407.

XXXIX. Liu, M.; Johnston, B. and Snaith, J. (2013). "Efficient planar heterojunction perovskite solar cells by vapour deposition". Nature 501 (7467): 395–398.

XL. Marinova, N., Tress, W., Humphry-Baker, R., Dar, M. I., Bojinov, V., Zakeeruddin, S. M., & Grätzel, M. (2015). Light harvesting and charge recombination in $CH_3NH_3PbI_3$ perovskite solar cells studied by hole transport layer thickness variation. ACS nano, 9(4), 4200-4209.

XLI. Meehan, C. (2014). "Getting the lead out of Perovskite Solar Cells". Solar Reviews.

XLII. Memming, R., and Bahnemann, D. (2015). Semiconductor electrochemistry. John Wiley & Sons.

XLIII. Minemoto, T. and Murata, M., (2014). "Device modeling of perovskite solar cells based on structural similarity with thin film inorganic semiconductor solar cells". Journal of Applied Physics 116 (5): 054505.

XLIV. Mosconi, E.; Amat, A.; Nazeeruddin, K.; Grätzel, M. and Angelis, F. (2013). "First-Principles Modeling of Mixed Halide Organometal Perovskites for Photovoltaic Applications". The Journal of Physical Chemistry C 117 (27): 13902–13913.

XLV. Nie, W.; Tsai, H.; Asadpour, R.; Blancon, J.; Neukirch, J.; Gupta, G.; Crochet, J.; Chhowalla, M. and Tretiak, S., (2015). "High-efficiency solution-processed perovskite solar cells with millimeter-scale grains". Science 347 (6221): 522–525. ISSN 0036-8075.

XLVI. Noel, K.; Stranks, D.; Abate, A.; Wehrenfennig, C.; Guarnera, S.; Haghighirad, A.; Sadhanala, A.; Eperon, E.; Pathak, K.; Johnston, B.; Petrozza, A.; Herz, M. and Snaith, J. (2014). "Lead-free organic–inorganic tin halide perovskites for photovoltaic applications"; Energy & Environmental Science 7 (9): 3061.

XLVII. Noel, N. K., Abate, A., Stranks, S. D., Parrott, E. S., Burlakov, V. M., Goriely, A., & Snaith, H. J. (2014). Enhanced photoluminescence and solar cell performance via Lewis base passivation of organic–inorganic lead halide perovskites. ACS nano, 8(10), 9815-9821.

XLVIII. Noh, H.; Im, H.; Heo, H.; Mandal, N. and Seok, I. (2013). "Chemical Management for Colorful, Efficient, and Stable Inorganic–Organic Hybrid Nanostructured Solar Cells". Nano Letters 13 (4).

XLIX. O'Regan, B. C., Barnes, P. R., Li, X., Law, C., Palomares, E., & Marin-Beloqui, J. M. (2015). Optoelectronic studies of methylammonium lead iodide perovskite solar cells with mesoporous TiO2: separation of electronic and chemical charge storage, understanding two recombination lifetimes, and the evolution of band offsets during J–V hysteresis. Journal of the American Chemical Society, 137(15), 5087-5099.

L. Oga, H., Saeki, A., Ogomi, Y., Hayase, S., & Seki, S. (2014). Improved understanding of the electronic and energetic landscapes of perovskite solar cells: high local charge carrier mobility, reduced recombination, and extremely shallow traps. Journal of the American Chemical Society, 136(39), 13818-13825.

LI. Pekola, J. P., Saira, O. P., Maisi, V. F., Kemppinen, A., Möttönen, M., Pashkin, Y. A., & Averin, D. V. (2013). Single-electron current sources: Toward a refined definition of the ampere. Reviews of Modern Physics, 85(4), 1421.

LII. Roche, B., Riwar, R. P., Voisin, B., Dupont-Ferrier, E., Wacquez, R., Vinet, M., & Jehl, X. (2013). A two-atom electron pump. Nature communications, 4, 1581.

LIII. Roy, S., & Bagchi, B. (1994). Time dependent solution of generalized Zusman model of outersphere electron transfer reactions: Applications to various experimental situations. The Journal of chemical physics, 100(12), 8802-8816.

LIV. Saliba, M.; Tan, W.; Sai, H.; Moore, T.; Scott, T.; Zhang, W.; Estroff, A.; Wiesner, U. and Snaith, J. (2014). "Influence of Thermal Processing Protocol upon the Crystallization and Photovoltaic Performance of Organic–Inorganic Lead Trihalide Perovskites". The Journal of Physical Chemistry C 118 (30): 17171–17177.

LV. Sanchez, R. S., Gonzalez-Pedro, V., Lee, J. W., Park, N. G., Kang, Y. S., Mora-Sero, I., & Bisquert, J. (2014). Slow dynamic processes in lead halide perovskite solar cells. Characteristic times and hysteresis. Journal of Physical Chemistry Letters, 5(13), 2357-2363.

LVI. Sha, E.; Ren, X.; Chen, L.; and Choy, H. (2015), "The efficiency limit of $CH_3NH_3PbI_3$ perovskite solar cells". Appl. Phys. Lett. 106 (22): 221104.

LVII. Shao, Y., Xiao, Z., Bi, C., Yuan, Y., & Huang, J. (2014). Origin and elimination of photocurrent hysteresis by fullerene passivation in $CH_3NH_3PbI_3$ planar heterojunction solar cells. Nature communications, 5.

LVIII. Sivaram, V.; Stranks, D. & Snaith, J. (2015). "Outshining Silicon". Scientific American: 44 - 46.

LIX. Snaith, J. (2013). "Perovskites: The Emergence of a New Era for Low-Cost, High-Efficiency Solar Cells". The Journal of Physical Chemistry Letters 4 (21): 3623–3630.

LX. Snaith, J.; Abate, A.; Ball, M.; Eperon, E.; Leijtens, T.; Noel, K.; Wang, T.; Wojciechowski, K.; Zhang, W. and Zhang, W. (2014). "Anomalous Hysteresis in Perovskite Solar Cells". The Journal of Physical Chemistry Letters 5 (9): 1511–1515.

LXI. Stranks, D.; Eperon, E.; Grancini, G.; Menelaou, C.; Alcocer, M.; Leijtens, T.; Herz, M. and Petrozza, A. (2013). "Electron-Hole Diffusion Lengths Exceeding 1 Micrometer in an Organometal Trihalide Perovskite Absorber". Science 342 (6156): 341–344.

LXII. Sun, X.; Asadpour, R.; Nie, W.; Mohite, A. and Alam, A. (2015). "A Physics-Based Analytical Model for Perovskite Solar Cells". IEEE Journal of Photovoltaics 5 (5): 1389–1394. ISSN 2156-3381.

LXIII. Tan, W.; Moore, T.; Saliba, M.; Sai, H.; Estroff, A.; Hanrath, T.; Snaith, J. and Wiesner, U, (2014). "Thermally Induced Structural Evolution and Performance of Mesoporous Block Copolymer-Directed Alumina Perovskite Solar Cells". ACS Nano 8 (5): 4730–4739.

LXIV. Tress, W., Marinova, N., Moehl, T., Zakeeruddin, S. M., Nazeeruddin, M. K., & Grätzel, M. (2015). Understanding the rate-dependent J–V hysteresis, slow time component, and aging in $CH_3NH_3PbI_3$ perovskite solar cells: the role of a compensated electric field. Energy & Environmental Science, 8(3), 995-1004.

LXV. Umari, P.; Mosconi, E. and Angelis, D. (2014). "Relativistic GW calculations on $CH_3NH_3PbI_3$ and CH3NH3SnI3 Perovskites for Solar Cell Applications". Scientific Reports 4.

LXVI. Unger, L.; Hoke, T.; Bailie, D.; Nguyen, H.; Bowring, R.; Heumuller, T.; Christoforo, G. and McGehee, D. (2014). "Hysteresis and transient behavior in current-voltage measurements of hybrid-perovskite absorber solar cells". Energy & Environmental Science 7 (11): 3690–3698.

LXVII. Wang, U. (2014). "Perovskite Offers Shot at Cheaper Solar Energy". Wall Street Journal.

LXVIII. Wei, J., Zhao, Y., Li, H., Li, G., Pan, J., Xu, D., & Yu, D. (2014). Hysteresis analysis based on the ferroelectric effect in hybrid perovskite solar cells. The journal of physical chemistry letters, 5(21), 3937-3945.

LXIX. Wilcox, K. (2014). "Solar Researchers Find Promise in Tin Perovskite Line". Civil Engineering.

LXX. Wilczek, F. (2014). Majorana and condensed matter physics. arXiv preprint arXiv:1404.0637.

LXXI. Xiao, Z.; Bi, C.; Shao, Y.; Dong, Q.; Wang, Q; Yuan, Y.; Wang, C.; Gao, Y. and Huang, J. (2014). "Efficient, High Yield Perovskite Photovoltaic Devices Grown by Interdiffusion of Solution-Processed Precursor Stacking Layers". Energy & Environmental Science 7 (8): 2619.

LXXII. Xie, F. X., Zhang, D., Su, H., Ren, X., Wong, K. S., Grätzel, M., & Choy, W. C. (2015).

LXXIII. Vacuum-assisted thermal annealing of CH3NH3PbI3 for highly stable and efficient perovskite solar cells. ACS nano, 9(1), 639-646.

LXXIV. Yang, B.; Dyck, O.; Poplawsky, J.; Keum, J.; Puretzky, A.; Sanjib, D.; Ivanov, I.; Rouleau, C.; Duscher, G.; Geohegan, D. and Xiao, K. (2015). "Perovskite Solar Cells with Near 100% Internal Quantum Efficiency Based on Large Single Crystalline Grains and Bulk Heterojunctions". J. Am. Chem. Soc. 137 (29): 9210–9213.

LXXV. You, J.; Hong, Z.; Yang, M.; Chen, Q; Cai, M; Song, T; Chen, C.; Lu, S. and Liu, Y. (2014). "Low-Temperature Solution-Processed Perovskite Solar Cells with High Efficiency and Flexibility". ACS Nano 8 (2): 1674–1680. ISSN 1936-0851.

LXXVI. Zhao, Y., & Zhu, K. (2014). CH3NH3PbCl-assisted one-step solution growth of $CH_3NH_3PbI_3$: structure, charge-carrier dynamics, and photovoltaic properties of perovskite solar cells. The Journal of Physical Chemistry C, 118(18), 9412-9418.

LXXVII. Zhou, H.; Chen, Q.; Li, G.; Luo, S.; Song, T..; Duan, H.; Hong, Z.; You, J.; Liu, Y. and Yang, Y. (2014). "Interface engineering of highly efficient perovskite solar cells". Science 345 (6196): 542–546.

LXXVIII. Zhou, Y.; Yang, M.; Wu, W.; Vasiliev, L.; Zhu, K. and Padture, P. (2015). "Room-temperature crystallization of hybrid-perovskite thin films via solvent–solvent extraction for high-performance solar cells". J. Mater. Chem. A 3 (15): 8178–8184.

LXXIX. 78. Zuo, L., Gu, Z., Ye, T., Fu, W., Wu, G., Li, H., & Chen, H. (2015). Enhanced photovoltaic performance of $CH_3NH_3PbI_3$ perovskite solar cells through interfacial engineering using self-assembling monolayer. Journal of the American Chemical Society, 137(7), 2674-2679.